New Insights into the High-Performance Black Phosphorus Anode for Lithium-Ion Batteries

Minsi Li, Weihan Li, Yongfeng Hu, Andrey A. Yakovenko, Yang Ren, Jing Luo, William M. Holden, Mohsen Shakouri, Qunfeng Xiao, Xuejie Gao, Feipeng Zhao, Jianwen Liang, Renfei Feng, Ruying Li, Gerald T. Seidler, Frank Brandys, Ranjith Divigalpitiya, Tsun-Kong Sham,* and Xueliang Sun*

Black phosphorus (BP) is a promising anode material in lithium-ion batteries (LIBs) owing to its high electrical conductivity and capacity. However, the huge volume change of BP during cycling induces rapid capacity fading. In addition, the unclear electrochemical mechanism of BP hinders the development of rational designs and preparation of high-performance BP-based anodes. Here, a high-performance nanostructured BP–graphite–carbon nanotubes composite (BP/G/CNTs) synthesized using ball-milling method is reported. The BP/G/CNTs anode delivers a high initial capacity of 1375 mA h g^{-1} at 0.15 A g^{-1} and maintains 1031.7 mA h g^{-1} after 450 cycles. Excellent high-rate performance is demonstrated with a capacity of 508.1 mA h g^{-1} after 3000 cycles at 2 A g^{-1}. Moreover, for the first time, direct evidence is provided experimentally to present the electrochemical mechanism of BP anodes with three-step lithiation and delithiation using ex situ X-ray diffraction (XRD), ex situ X-ray absorption spectroscopy (XAS), ex situ X-ray emission spectroscopy, operando XRD, and operando XAS, which reveal the formation of Li$_3$P$_7$, LiP, and Li$_3$P. Furthermore, the study indicates an open-circuit relaxation effect of the electrode with ex situ and operando XAS analyses.

1. Introduction

Lithium-ion batteries (LIBs) have been used in portable devices since 1991.[1] Due to its high storage capacity, good cycling performance, and high energy density, LIBs have become the most common energy storage device in cell phones, laptops, and electrical vehicles.[2] The cathode materials in commercial LIBs are normally well-developed LiCoO$_2$, LiFePO$_4$, and LiMn$_2$O$_4$.[3] However, the commonly used anode, such as carbon-based material has insufficient capacity for daily usage.[4] Thus, it is crucial to develop new anode materials with higher capacity and longer cycle life.

Phosphorus has been known to be a decent anode material for LIBs for decades, owing to its remarkable theoretical capacity (2592 mA h g^{-1}).[5] It has three allotropes: white phosphorus (WP), red phosphorus (RP), and black phosphorus (BP). WP is chemically unstable and spontaneously ignites in air, which cannot be used in LIBs due to the safety issues. RP and BP are chemically more stable than WP. They have been explored as anode materials in LIBs. However, despite the high theoretical capacity of RP and BP, they face several challenges, such as extremely large volume change of over 300% during charging and discharging processes, which can cause pulverization of the electrode material and induce rapid capacity fading of the battery.[6,7] To prevent the electrode material from pulverization during cycling, one

M. Li, Dr. W. Li, X. Gao, Prof. T.-K. Sham
Department of Chemistry and Soochow-Western Centre for Synchrotron Radiation Research
University of Western Ontario
London, Ontario N6A 5B7, Canada
E-mail: tsham@uwo.ca

M. Li, Dr. W. Li, J. Luo, X. Gao, F. Zhao, Dr. J. Liang, R. Li, Prof. X. Sun
Department of Mechanical and Materials Engineering
University of Western Ontario
London, Ontario N6A 5B9, Canada
E-mail: xsun9@uwo.ca

Dr. Y. Hu, Dr. M. Shakouri, Dr. Q. Xiao, Dr. R. Feng
Canadian Light Source
44 Innovation Boulevard, Saskatoon, Saskatchewan S7N 2V3, Canada

Dr. A. A. Yakovenko, Dr. Y. Ren
Advanced Photon Source
Argonne National Laboratory
Argonne, IL 60439, USA

Dr. W. M. Holden
easyXAFS LLC
Renton, WA 98057, USA

Prof. G. T. Seidler
Physics Department
University of Washington
Seattle, WA 98195-1560, USA

Prof. F. Brandys, Prof. R. Divigalpitiya
3M Canada Company
1840 Oxford Street East, London, Ontario N5V 3R6, Canada

**ADVANCED
SCIENCE NEWS**

www.advancedsciencenews.com

**ADVANCED
MATERIALS**

www.advmat.de

effective strategy is to prepare nano-phosphorus–carbon composites.[8] There are two main methods to synthesize phosphorus–carbon composites, vaporization–condensation[9–11] and ball-milling.[11–13] Compared to the vaporization–condensation method, ball-milling method is more suitable for industrial application, which can realize large-scale and low-cost preparation. Compared to RP, BP is the more promising anode material which might help resolving the issues of current commercial graphite-based anodes. BP has more stable thermodynamics, higher carrier mobility, and higher electrical conductivity and thus is likely to show remarkable electrochemical performance as anode materials in LIBs.[14–16] Sun and Haghighat-Shishavan ball-milled RP with graphite and carbon nanotubes, respectively with high-energy mechanical milling machine and RP was transferred to BP during the process. The resulting material shows a good cyclability of 1849 and 1681 mA h g^{-1} after 100 and 400 cycles, respectively.[17,18] Most recently, Jin et al. presented a BP–G/PANI composite and achieved robust high-rate capacity and cycling stability. The designed composite delivers a capacity of 440 mA h g^{-1} after 2000 cycles at 13 A g^{-1}.[19] Based on the previous studies, preparing BP–carbon composite through a ball-milling process could be considered an effective approach to improve the electrochemical performance of BP-based anode materials.

In addition to the well-designed structure, it is also important to understand the mechanism of how phosphorus interacts with Li$^+$ during discharge and charge, in order to realize reasonable structural design and preparation of materials and eventually improve the overall electrochemical performance. It has been previously confirmed by X-ray diffraction (XRD) that phosphorus will alloy with Li$^+$, forming LiP, Li$_2$P, and then Li$_3$P when fully discharged; and the discharge products transform back to phosphorus when fully charged.[10,12,20,21] Recently, this process is also supported by Jin et al. through in situ X-ray absorption spectroscopy (XAS).[19] The theoretical studies, however, showed that other Li species (e.g., LiP$_7$, Li$_3$P$_7$, Li$_4$P$_3$) may also form during lithium insertion/extraction, and Li$_2$P is not considered as a stable structure during the cycling.[5,22] Thus, the theoretical and the experimental results are inconsistent. Therefore, to understand the electrochemical mechanism thoroughly, a more solid study should be carried out using comprehensive techniques to track not only the average crystal structure evolution but also the local chemical environment alteration.

Herein, we report a composite of black phosphorus, graphite, and single-walled carbon nanotubes (BP/G/CNTs) as a high-performance anode and studied the detailed electrochemical mechanism by ex situ and operando synchrotron-based analytical techniques. The BP was milled with graphite and CNTs (50 wt% BP, 40 wt% graphite, 10 wt% CNTs) using a planetary ball-milling machine. After 120 h ball-milling, BP was milled into nanosized material, imbedded in a matrix of graphite and CNTs. The BP/G/CNTs composite shows several advantages: 1) the introduction of carbon materials can improve the electrical conductivity of BP; 2) graphite accommodates the volume change of BP during cycling, preventing the pulverization of the material; 3) the CNTs not only stabilize the structure of the composite, but also provide pathways for electrons and Li$^+$ ions. Benefiting from the unique structure, the BP/G/CNTs anode

delivers a remarkable initial charge capacity of 1375 mA h g^{-1} at 0.15 A g^{-1} and long cycle life with 1031.7 mA h g^{-1} after 450 cycles. Moreover, it also shows great high-current performance with a capacity of 719 mA h g^{-1} after 1000 cycles and 508.1 mA h g^{-1} after 3000 cycles at a current density of 2 A g^{-1}. Although the electrochemical performance of BP-based anode materials in LIBs has been already improved significantly by other works, the achievement of overall high performance and stability at high current densities beyond 1 A g^{-1} is rare (Table S1, Supporting Information).

In addition to the remarkable electrochemical performance, we also experimentally clarify the electrochemical mechanism of BP during cycling. We for the first time confirm the complete electrochemical mechanism of BP anode during lithiation and delithiation. The electrochemical products/intermediates during cycling are confirmed by ex situ XRD, XAS, and X-ray emission spectroscopy (XES), operando XRD, and operando XAS analyses. Synchrotron-based XAS and XES techniques involve electron excitation and X-ray fluorescence emission, which can track the electronic structure and local chemical environment of the interested materials.[23,24] XAS and XES can provide information on the local structures that XRD cannot measure and are suitable to study the electrochemical mechanism of phosphorus-based anode materials in LIBs. Combining the ex situ XAS and XES, operando XRD, operando XAS, and ex situ XRD analyses, we provide direct evidence to unravel the step-by-step phase transformation of BP to Li$_3$P$_7$, LiP, and Li$_3$P, and their reversible conversion during charging. Moreover, we also precisely observe the open-circuit relaxation effect of the BP-based electrode by comparing ex situ and operando XRD and XAS. Operando analyses are particularly important for understanding the real-time behaviors in LIBs. This work can provide a guide to achieve high-performance anode material and understand the electrochemical mechanism of electrode materials in LIBs.

2. Results and Discussion

The BP/G/CNTs composite (**Figure 1**a) was prepared by ball-milling the mixture of BP, graphite, and single-walled CNTs at a weight ratio of 5:4:1 under 550 rpm for 120 h. The particle size was decreased from over 20 μm to 50–200 nm (Figure S1a,b, Supporting Information). The nanosized effect not only stabilizes the structure, preventing it from cracking during volume change, but also enhances the contact between the conductive materials and active materials.[25] The low magnification transmission electron microscope (TEM) image in Figure 1c further confirms that the particle size of BP/G/CNTs is in the range of 50–200 nm (Figure S1c, Supporting Information). Moreover, secondary particles with the size of 0.5–2 μm can be found as well, which could minimize the formation of solid-electrolyte interface (SEI) and provide internal spaces for phosphorus expansion.[26] Because of the specific nanosized secondary structure, the capacity and stability of BP/G/CNTs can be further improved. The high-resolution TEM (Figure 1b) clearly shows that the BP/G/CNTs composite particle consists of nanosized BP, graphite, and CNTs with excellent contact among them. Two different lattice spacings of 3.3 and 2.2 Å
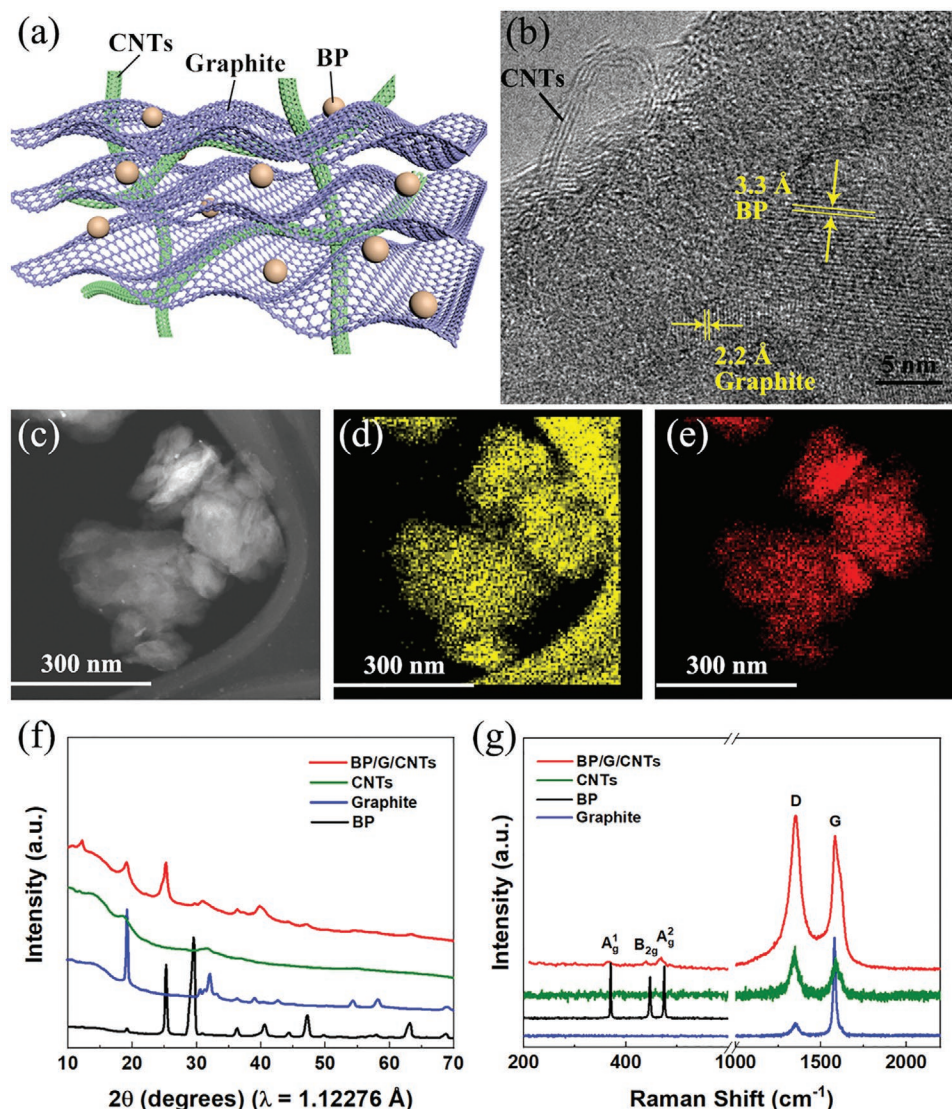
ADVANCED
SCIENCE NEWS
www.advancedsciencenews.com

ADVANCED
MATERIALS
www.advmat.de

Figure 1. a) Schematic of the BP/G/CNTs composite. b) HR-TEM of the BP/G/CNTs. c) Dark field TEM of the BP/G/CNTs and the corresponding d) C and e) P elemental maps in (c). f) XRD and g) Raman spectra of BP/G/CNTs compared with pristine BP, graphite flakes, and CNTs.

can be found in the image, corresponding to the (021) lattices of BP[16] and the (10$\bar{1}$0) plane of graphite,[19] respectively. More importantly, the particle size of BP was decreased to 5–10 nm, which will drastically reduce the possibility of the cracking during the volume change in the electrochemical process. After the ball-milling process, graphite will also be milled to small flakes (Figure S1d,f, Supporting Information). In addition, the ball-milling process will shorten the CNTs. However, the diameter and the structure of the CNTs are retained (Figure S1e,f, Supporting Information). As we showed in Figure 1a, the small graphite flakes connect and cover the nanosized BP particles to prevent them from pulverization due to the huge volume change during cycling. The CNTs can link the whole structure and provide fast pathways for Li+ transport. This well-designed structure is confirmed in the high resolution transmission electron microscope (HR-TEM) image in Figure 1b and will enhance the long cycle stability and rate performance of BP/G/

CNTs. Moreover, the elemental mapping demonstrates that nanosized BP was uniformly distributed in the G/CNTs matrix (Figure 1c–e and Figure S1g–i (Supporting Information)).

Figure 1f,g represents the XRD and Raman spectra of graphite flakes, CNTs, bulk BP, and BP/G/CNTs composite, respectively. In Figure 1f, the XRD patterns of BP (black), graphite flakes (blue), and CNTs (green) are consistent with the reference patterns.[27,28] The XRD pattern of BP/G/CNTs composite (red) shows characteristic peaks of BP, graphite, and CNTs, indicating intact crystal structures of the three precursors after ball-milling. The Raman spectrum of bulk BP shows three peaks at 359.8, 436.9, and 463.8 cm^{-1}, representing the A_g^1, B_{2g}, and A_g^2 vibrational modes, respectively.[29] Raman peaks at 1354 and 1583 cm^{-1} are represented as the D-band and G-band of graphite and CNTs, describing the defects and disorder portions and graphitic layers.[30] In the Raman spectrum of BP/G/CNTs, signals from both bulk BP and graphite flakes
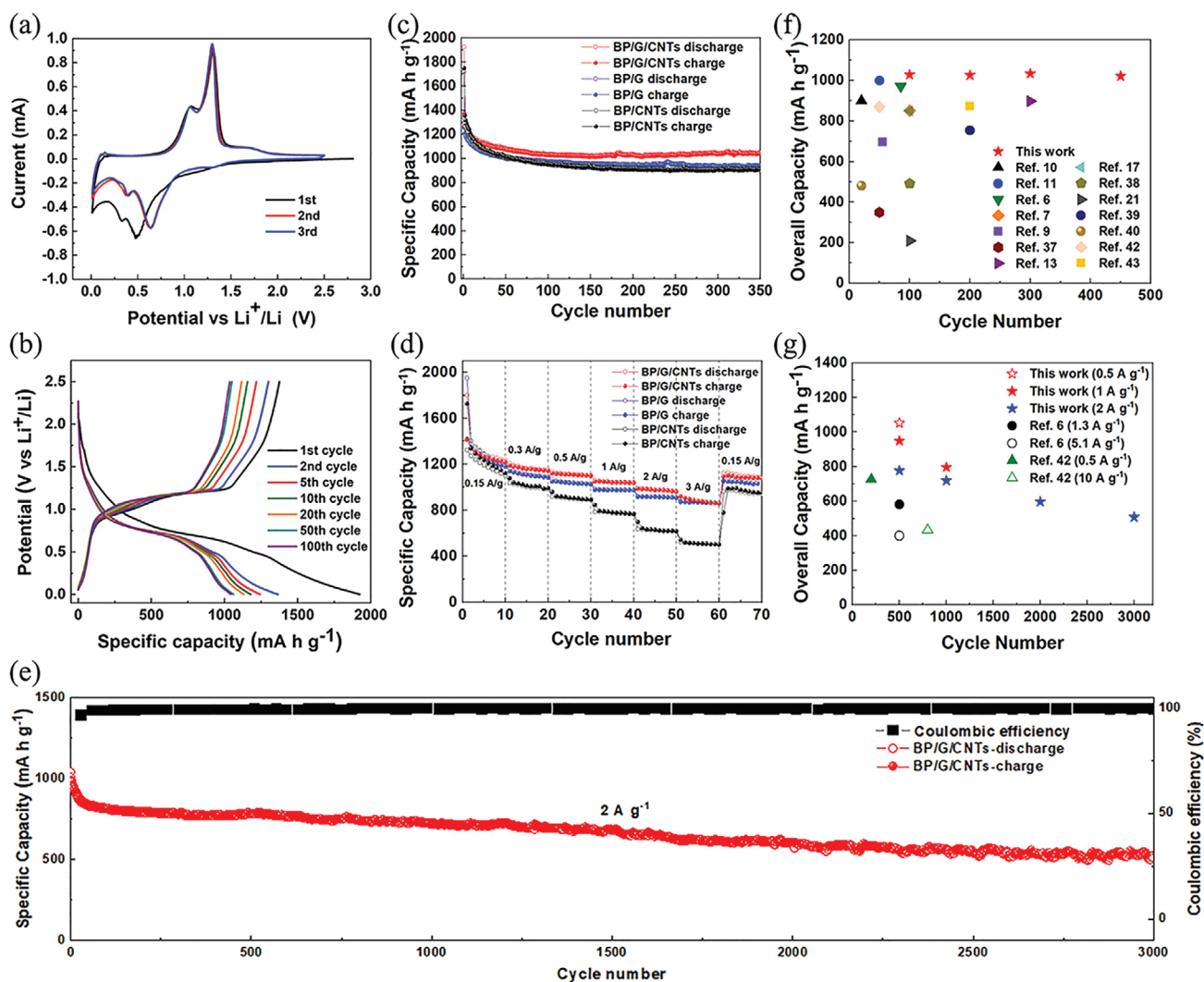
Figure 2. a) Cyclic voltammograms of the BP/G/CNTs anode at a scan rate of 0.2 mV s^{-1}. b–d) Electrochemical performance of BP/G/CNTs cycled between 0.01 and 2.5 V versus Li$^+$/Li: (b) voltage profiles of BP/G/CNTs at 0.15 A g^{-1}, (c) Cycling performance of BP/G/CNT anode compared with BP/G and BP/CNTs anodes at 0.15 A g^{-1}, (d) capacity of BP/G/CNTs compared with BP/G and BP/CNTs as a function of cycling rate (0.15–3A g^{-1}). e) Capacity and Coulombic efficiency during cycling of BP/G/CNTs anode at 2 A g^{-1} after 5 initial cycles at low current density of 0.15 A g^{-1}. Overall capacity and cycling stability compared with other reported RP- and BP-based anode materials at current densities f) lower than 0.5 A g^{-1} and g) above 0.5 A g^{-1}. The data and current density of each material are summarized in Table S1 (Supporting Information).

are observed, confirming the composite nature of the obtained material. The peaks from BP are weaker than that in bulk BP, which is because the bulk BP was nanosized after ball-milling.[6] In addition, the A$_g^1$, B$_{2g}$, and A$_g^2$ vibrations of BP in the BP/G/CNTs composite shift to higher frequencies, giving evidence for the thinning of BP after ball-milling.[31] The intensity ratio of D-band and G-band ($R_I = I_D/I_G$) of BP/G/CNTs drastically increases compared to that of the graphite flakes, indicating that more defects are created on the carbon-based materials during the synthesis process.[32] Thus, comparing the Raman spectrum of BP/G/CNTs with those of bulk BP, graphite flakes, and CNTs, the composite after ball-milling process shows increased disorder and defects in both BP and carbon-based materials.

The electrochemical performances of BP/G/CNTs are shown in **Figure 2**. Figure 2a shows the cyclic voltammograms (CV) curves of a BP/G/CNTs electrode with Li metal reference elec-

trode in the voltage window of 0–2.5 V. In the cathodic scan of the curve, five obvious peaks were observed. The peaks at 1.109, 0.783, and 0.483 V were associated with the three-step reactions of the lithiation process of BP.[6,12] The broad peak at 1.43–0.95 V could be attributed to both SEI formation and the first step lithiation since this peak was narrowed at 2nd and 3rd scans. While peaks at 0.325 and 0.01 V can be attributed to the lithium insertions into graphite and CNTs.[33] During anodic scan, the tiny peak at ≈0.2 V was ascribed to the lithium extraction from graphite/CNTs and the three peaks at 1.056, 1.311, and 1.668 V show the reversible delithiation process of BP (Figure S2a, Supporting Information). After the 1st cycle, the CV curves of the 2nd and 3rd cycles showed high reversibility and good cyclability of BP/G/CNTs in LIBs.

Figure 2b shows the voltage profiles of the BP/G/CNTs anode at a current of 0.15 A g^{-1} between 0.01 and 2.5 V versus (Li$^+$/Li).

**ADVANCED
SCIENCE NEWS**
www.advancedsciencenews.com

**ADVANCED
MATERIALS**
www.advmat.de

The irreversible capacity of the initial cycle was due to the formation of SEI. Corresponding to CV curves, the voltage profile shows a clear three-step reaction between BP and Li^+ with three plateaus for both discharge and charge curves. The plateaus were observed at 1.35–1.00, 0.90–0.60, and 0.60–0.47 V during discharging, and 0.88–1.07, 1.07–1.24, and 1.25–1.70 V during charging, respectively, which is in good correspondence with the CV curves. In addition, compared between the voltage profile curves of BP/G/CNTs and G/CNTs, the change of the slope below 0.3 V of the BP/G/CNTs voltage profile curve might be contributed by graphite and CNTs, which is corresponding to the curve of G/CNTs (Figure S2b, Supporting Information). The cycling performance of BP/G/CNTs was compared with BP/G and BP/CNTs, as shown in Figure 2c. The BP/G/CNTs showed the best cycling stability, delivering an initial charge capacity of 1375 mA h g^{-1} which was more than twice of the capacity of G/CNTs (657.1 mA h g^{-1}) (Figure S3a, Supporting Information). Based on the weight ratio of BP (Figure S3b, Supporting Information), the specific initial capacity contribution of BP is 2522 mA h g^{-1}, which is close to the theoretical capacity. The initial Coulombic efficiency is as high as 71.45% and increases to >98% in 5 cycles, showing the good cycling stability of the BP/G/CNTs electrode for LIBs. The capacity remained 1040.9 mA h g^{-1} after 350 cycles. After 450 cycles, the capacity of BP/G/CNTs still maintained 1031.7 mA h g^{-1}, which is 75% of the initial charge capacity with the low decay rate of 0.3% per cycle (Figure S4a, Supporting Information). The ratios of BP, graphite, and CNTs were adjusted for comparison. The result shows that BP/G/CNTs with the ratio 5:4:1 delivers the highest overall capacity after long cycle and shows the best cycling stability (Figure S5, Supporting Information). In addition, BP/G/CNTs also showed the best rate performances compared to BP/G and BP/CNTs (Figure 2d). The BP/G/CNTs anode demonstrated highly reversible capacities of 1185.6, 1119.5, 1049.1, 985.8, and 914.9 mA h g^{-1} at various current densities of 0.3, 0.5, 1, 2, and 3 A g^{-1}, respectively. The presence of both graphite and CNTs contributed to the remarkable cycling performance and rate performance of BP/G/CNTs composite. More specifically, the graphite component accommodated the volume change of BP during cycling, avoiding the pulverization of the material. The function of graphite can be confirmed by the scanning electron microscope (SEM) images of the electrodes before cycling, after discharged to D-0.001 V and after 1st cycle (Figure S6 and S7, Supporting Information). Both top view and side view of the SEM images of pure BP electrode show that the bulk BP is cracked during the cycling. More importantly, Figure S6e (Supporting Information) indicates that the active materials disconnect to the current collector after 1st cycle, which induces the capacity fading in LIBs. By contrast, although the volume expansion of BP can also be found in BP/G/CNTs after discharged to D-0.001 V, the introducing of graphite can accommodate that volume change and prevent the material from pulverization and disconnecting to the current collector. The CNTs component can provide pathways of electrons and Li^+ ions, improving the kinetics within the BP-based electrode (Figure S8, Supporting Information). Thus, BP/G/CNTs shows promising long cycle stability in LIBs.

Moreover, the BP/G/CNTs electrode demonstrated excellent cycling performance at high current densities. The specific

capacities remained 1009.4 mA h g^{-1} after 600 cycles at 0.5 A g^{-1} and 996 mA h g^{-1} after 1000 cycles at 1 A g^{-1}, corresponding to capacity retentions of 78% and 79%, respectively (Figure S4b,c, Supporting Information). Significantly, BP/G/CNTs showed ultralong cycling stability at a high current density of 2 A g^{-1}, remaining 719 mA h g^{-1} after 1000 cycles and 508.1 mA h g^{-1} after 3000 cycles (Figure 2e). The cycling stability of BP/G/CNTs under 1 A g^{-1} is not as good as that under 2 A g^{-1}, which is because the reaction between BP and Li^+ is more complete during the cycling under the current density of 1 A g^{-1}. To clarify, large portion of BP are involved in the reaction and influenced by the serious volume change during cycling under low current density, which can be proved by the higher overall capacity of BP/G/CNTs under 1 A g^{-1}. Overall, the ball-milled BP/G/CNTs displayed a remarkable capacity, good cycling stability, and high rate performance, which were due to the well-designed nanosized structure and the introduction of graphite flakes and CNTs. In addition, by comparing the electrochemical performance of BP in this work with most of the previous works, BP/G/CNTs still shows advanced overall capacity and long cycling stability at both low current density and high current densities (i.e., 0.5, 1, and 2 A g^{-1}) (Figure 2f,g and Table S1 (Supporting Information)).

To understand the electrochemical mechanism of BP-based anode materials in LIBs, we conducted XRD and synchrotron-based XAS and XES analyses to investigate the lithiation and delithiation processes of the BP/G/CNTs anode. By combining the operando XAS with ex situ XRD, XAS, and XES, Li–P alloying at different voltages during cycling was precisely tracked to unravel the electrochemical reaction mechanism. **Figure 3** shows the ex situ XRD, XAS, and XES results. In the voltage profiles (Figure 3a), 14 discharge/charge states were selected for the ex situ measurements. Based on the ex situ XRD results of the 7 states during discharge (Figure 3b), Li_3P_7 was detected at 0.75 V and subsequently Li_3P at 0.5 V. The presence of Li_3P_7 at 0.75 V can be further confirmed by HR-TEM image (Figure S9, Supporting Information), which clearly shows the (121) facet of Li_3P_7. The intensity of Li_3P peaks in XRD spectra increases after 0.5 V, indicating the further formation of Li_3P. However, the formation of amorphous LiP was also proposed in previous studies and theoretical works, which cannot be determined with confidence in the ex situ XRD.[5,22,34] Thus, other techniques that are sensitive to both crystalline and amorphous structures are required to understand the reaction between Li^+ and BP.

Figure 3c,d shows the ex situ P K-edge XAS spectra of BP/G/CNTs discharged and charged to certain voltages, acquired in fluorescence yield mode. The peak A at 2144.7 eV of the pristine sample originated from dipole transition from P 1s to states with P 3p character of BP.[35] The peaks B and C at 2150.1 and 2152.5 eV corresponded to the 1s–3p transition in P with higher oxidation states P(III) and P(V), respectively.[36] The intensities of P(III) and P(V) peaks were relatively low, which suggested the weak oxidation of BP during electrode preparation or transportation. During discharge (Figure 3c), Li^+ was gradually inserted into the BP structure and BP transforms to Li_3P, leading to the edge shift to lower photon energy accompanied by a reduction in intensity as the P 3p occupied densities of states increased. The peak position and intensity variation were related to the
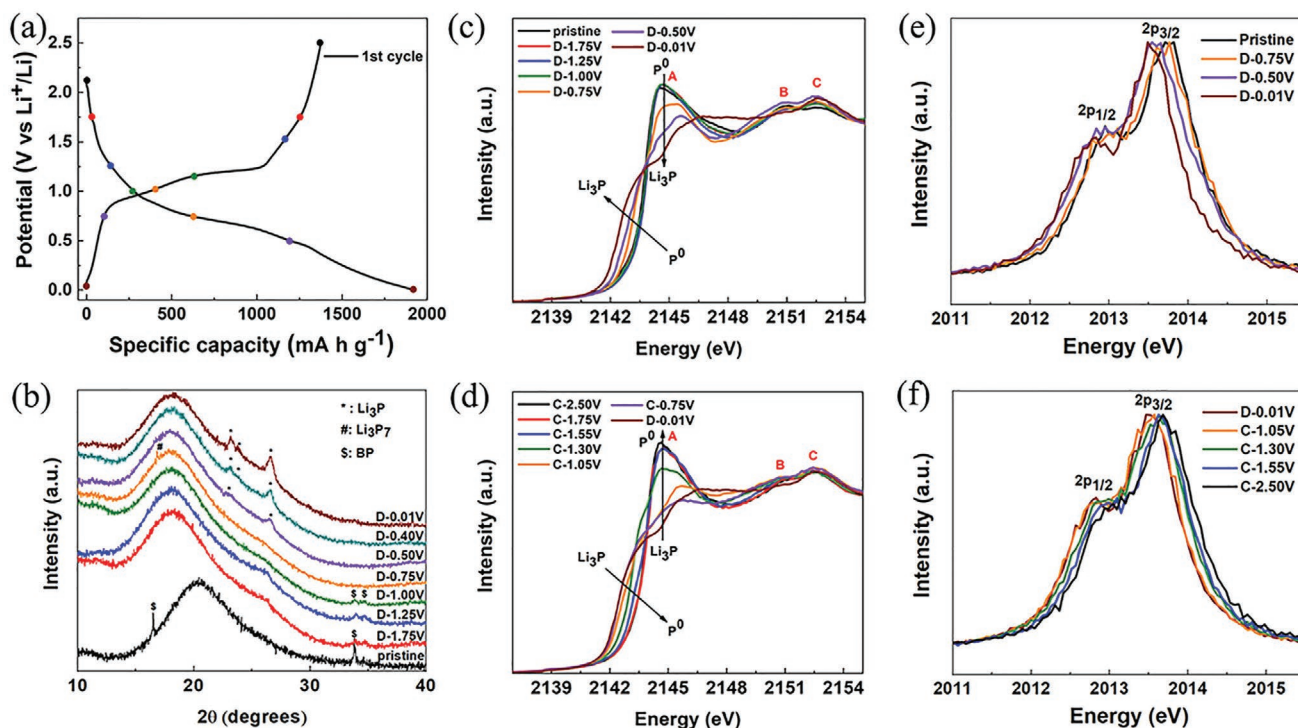
**ADVANCED
SCIENCE NEWS**

www.advancedsciencenews.com

**ADVANCED
MATERIALS**

www.advmat.de

Figure 3. a) Voltage profiles of the BP/G/CNTs anode with the corresponding discharge/charge states for measurements in (c) and (d). b) Ex situ XRD of the BP/G/CNTs anode during discharge. P K-edge ex situ XAS of BP/G/CNTs during c) discharge and d) charge. P Kα ex situ XES excited at 2148.7 eV photon energy of BP/G/CNTs during e) discharge and f) charge.

3p orbital state of BP, which is gradually filled by the electrons from the Li metal counter electrode. The shifts to lower energy can be clearly observed for samples discharged to 0.75, 0.5, and 0.01 V, which were consistent with the conclusion from the ex situ XRD results. Both ex situ XAS and XRD results confirm the existence of Li_3P_7 at 0.75 V and Li_3P at 0.5 V. In addition, the disappearance of the peak at 2144.7 eV and the lower energy shift of the sample at 0.01 V confirmed a full transformation to Li_3P after discharge. The ex situ XAS spectra during charging show a reversible trend with the gradual increase in absorption-edge energy and peak area (**Figure 4**d). The absorption-edge energy positions for the different discharge and charge states are compared in Figure S10a (Supporting Information). Same positions are shown for the pair of 0.75 V discharge (D-0.75 V) and 1.30 V charge (C-1.30 V) states and the pair of D-0.50 V/-C-1.05 V, indicating similar components at these states. However, the peak position at the state of C-1.55 V is absent among spectra of discharge states, which reveals a new component at C-1.55 V.

The change of the P electronic structure of BP/G/CNTs in LIBs at different discharge/charge states was tracked by P Kα XES (Figure 3e,f). The incident X-ray energy for the XES measurements was set at 2148.7 eV, which is above the threshold of the reduced states of P but lower than the absorption threshold of P(III), P(V), and PF_6^- which can minimize the fluorescence contribution from high P oxidation states and the electrolyte. It should be noted that the XES spectrometer has <1 eV energy resolution in this region. The XES spectra clearly show two peaks with intensity ratio of 2:1. The two peaks are the P Kα_1

and P Kα_2 X-ray fluorescence arising from transition from $2p_{3/2}$ and $2p_{2/1}$, respectively, decaying back to the P 1s core hole. It is apparent from Figure 3e,f that the same trend of shifts in the position of the P Kα_1 and Kα_2 occurred as that observed in P K-edge XAS. That is, the XES peaks shift to lower energy during discharge and to higher energy during charge, as a result of gain and loss of electrons, respectively, at the P site. The P Kα_1 and Kα_2 peak positions of pristine and C-2.50 V states are similar at 2010.56/2009.80 and 2010.49/2009.75 eV, respectively, which show high reversibility of the lithiation/del-ithiation process of BP nanoparticles during the initial cycle. The XES results are in excellent accordant with the results from ex situ XRD and XAS, showing that the charge redistribution occurs upon Li^+ insertion leading to the formation of Li_3P.

Due to the concerns associated with the ex situ XRD (not sensitive to amorphous phases) and XAS (possible formation of metastable phases), operando P K-edge XAS during cycling was investigated in a He-filled chamber in order to further confirm the electrochemical reaction mechanism of BP. Figure 4a shows the schematic of the operando XAS study, using fluorescence to track the electronic structure evolution of BP during cycling. One homemade coin cell with a mylar film window can allow incident X-ray to hit BP/G/CNTs anode and fluorescent X-ray to escape with electronic structure information. The operando XAS results (Figure 4b,c) show a similar trend in energy shifts and change in peak area as compared with the ex situ analyses. During discharge, the absorption edge gradually shifted to lower energy with decreasing peak area (Figure 4b). All discharge/charge states with absorption edge shifts in the
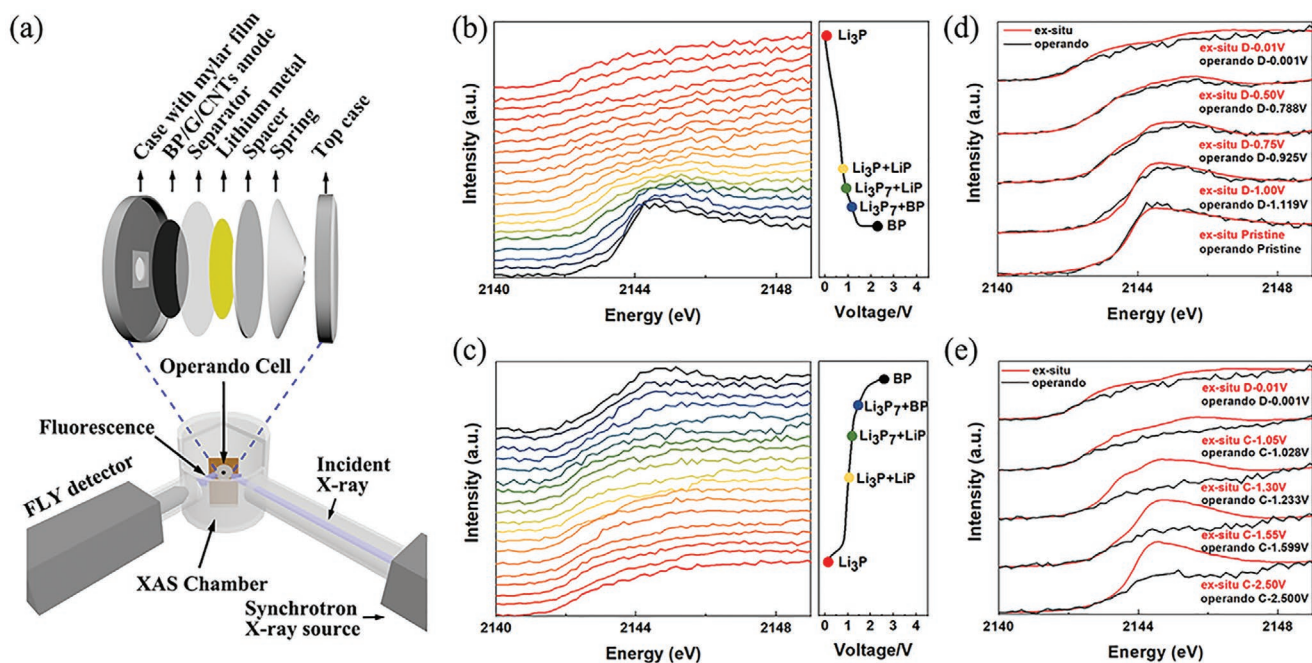
Figure 4. a) Schematic of the operando P K-edge XAS measurement setup. Operando P K-edge XAS of the BP/G/CNTs electrode during b) discharge (from bottom to top) and c) charge (from top to bottom). Comparison of ex situ and operando P K-edge XAS of BP/G/CNTs of d) discharge and e) charge.

spectra have been replotted in the bottom part of Figure S10b (Supporting Information) for a better viewing. As displayed by the operando XAS results, there are five distinct spectra with different absorption edges during discharge—operando pristine, D-1.119 V, D-0.925 V, D-0.788 V, and D-0.001 V (see bottom of Figure S10b in the Supporting Information). The operando and ex situ XAS spectra of pristine BP/G/CNTs are consistent, indicating the same composition of the operando pristine and ex situ pristine electrodes. The first shift of absorption edge during operando XAS measurements was found at operando D-1.119 V. This means a new phase formation at this voltage during discharge. When the electrode was discharged to D-0.925 V, another shift of absorption edge occurred. The absorption edge of operando D-0.925 V was consistent with the ex situ D-0.75 V, indicating existence of Li_3P_7 at operando D-0.925 V. Based on the XRD spectrum of ex situ D-0.75 V, no XRD characteristics belonging to BP were found when the electrode is discharged to both ex situ D-0.75 V and operando D-0.925 V. This means that BP was fully converted to Li_3P_7 at this voltage. Thus, we suggest that the shift of absorption edge at operando D-1.119 V is referred to the initial formation of Li_3P_7. This speculation can be supported by the theoretical study of Mayo et al.,[5] which suggested that the structure of Li_3P_7 will be found between 1.10 and 1.20 V during BP discharge. This theoretical study also predicted that BP transforms to LiP_7 first at 1.5 V during discharge. However, no absorption edge shift was found in the XAS spectra around operando D-1.5 V. Therefore, we assume that LiP_7 may not exist during the cycling of BP/G/CNTs. The third and fourth shifts of absorption edge among operando XAS spectra appear at D-0.788 V and D-0.001 V, equivalent to the absorption edge of ex situ D-0.50 V and D-0.01 V, respectively. Thus, by analyzing the ex situ

XRD spectra of D-0.50 V and D-0.01 V, the absence of Li_3P_7 and occurrence of Li_3P can be confirmed when the electrode was discharged to 0.788 and 0.001 V (D-0.788 V and D-0.001 V). In addition, both the absorption energy shift in the operando XAS spectra of D-0.788 V/D-0.001 V and the peak intensity increase in ex situ XRD spectra of the D-0.50 V to D-0.01 V samples indicated that Li_3P was first formed at 0.788 V and reached the highest content at 0.001 V during discharge. This conclusion is also consistent with the theoretical study.[5] Moreover, since Li_3P_7 was only observable from the operando measurement at D-0.925 V, we suggest that an intermediate step from Li_3P_7 to an amorphous Li–P phase occurred between operando D-0.925 V and operando D-0.788 V, followed by further conversion to Li_3P at operando D-0.788 V and reached final discharge products at D-0.001 V. Based on the calculated results of the average voltages relative to Li metal of different Li–P composites, the amorphous Li–P phase during discharge might be LiP, which will be formed at 0.9 V in the theoretical work. In conclusion, the electrochemical reaction process of BP/G/CNTs during discharge will be

$$BP \rightarrow Li_3P_7 \,(1.119-0.925V) \rightarrow LiP \,(0.925-0.788V) \\ \rightarrow Li_3P \,(0.788-0.001V) \tag{1}$$
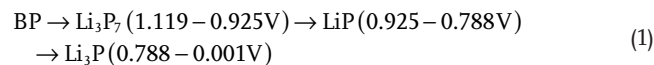
This process can be further supported by calculating the capacity contribution of P at different voltages. It shows that the P capacity contribution at D-1.119 V, D-0.925 V, and D-0.788 V are 2.6%, 11.0%, and 26.5% of the fully discharged capacity, respectively. The capacities at D-0.925 V and D-0.788 V can be ascribed to the Li^+-insertion capacity of Li_3P_7 and LiP, respectively.

**ADVANCED
SCIENCE NEWS**
www.advancedsciencenews.com

**ADVANCED
MATERIALS**
www.advmat.de

The operando XAS spectra during charging revealed the opposite trend of increasing white line area and absorption edge energy shift (Figure 4c), compared with that during the discharging process. This observation indicates a reversible process in BP/G/CNTs electrode during cycling. The spectra with absorption edge shifts are compared at top of Figure S10b (Supporting Information). Similar to the discharge result, the spectra during charging also show five different absorption edge positions for different species at D-0.001 V, C-1.028 V, C-1.233 V, C-1.599 V, and C-2.500 V. These XAS spectra also show exact correspondence to the ex situ XAS spectra during charge (Figure 4e). By comparing the absorption edge between the operando XAS spectra of BP/G/CNTs at different charge and discharge states, we conclude that the absorption edges of the spectra of the D-0.001 V, C-1.028 V, C-1.233 V, C-1.599 V, and C-2.500 V states during charge are correspondent with the spectra of D-0.001 V, D-0.788 V, D-0.925 V, D-1.119 V, and pristine states during discharge, respectively. The same component was formed in the electrode at each pair of charge/discharge states. Thus, during charge, Li_3P started to transform to LiP at C-1.028 V, then formed a mixture of Li_3P and LiP. The transformation completed at C-1.233 V when the LiP further converted to Li_3P_7. Finally, lithium was extracted from Li_3P_7, forming BP. This process started at C-1.599 V. In conclusion, the electrochemical reaction process of BP/G/CNTs during charge should be

$$Li_3P \rightarrow LiP\,(1.028-1.233V) \rightarrow Li_3P_7\,(1.233-1.599V) \\ \rightarrow BP\,(1.599-2.500V) \qquad (2)$$
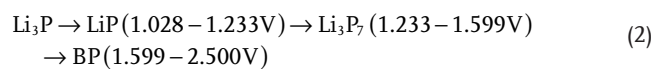
Additionally, the operando and ex situ XAS reveal different voltages when the electrode reached to the same lithiation/delithiation state (Figure 4d,e), which was likely due to open-circuit relaxation effect of the electrode as discussed previously.[37]

The operando XRD measurement was investigated to further confirm the observations in ex situ XRD, ex situ XAS, and operando XAS (**Figure 5**). The design of the operando XRD cell is similar to that of operando XAS (Figure 5a). However, a 3 mm hole was created in the middle of the lithium metal and the spencer to eliminate the interferential signals. A high energy X-ray with a wavelength of 0.24145 Å was used to obtain the diffraction of the electrode, and the scattered X-ray was recorded with a Varex 4343CT 2D detector. The operando XRD results are shown in Figure 5b,c. The results clearly show the phase transformations of BP during cycling at different voltage stages, which are corresponding with the results of operando XAS. During discharge, BP starts to transform to Li_3P_7 at 1.206 V. After the transform, both BP and Li_3P_7 exist between D-1.206 V and D-0.893 V. Similarly, the coexistence of Li_3P_7 and LiP, LiP and Li_3P can be found from D-0.893 V to D-0.799 V and D-0.799 V to D-0.001 V, respectively. This indicates that the phase transform voltage from Li_3P_7 to LiP and LiP to Li_3P are D-0.893 V and D-0.799 V. Finally, the transformation from BP to Li_3P fully finished at D-0.001 V. Similar to the discharge results, the operando XRD spectra during charge show the reversible trend. Li_3P starts to transform to LiP, Li_3P_7, and BP gradually at C-0.840 V, C-1.227 V, and C-1.623 V. The coexistence of the adjacent phases is revealed in the spectra from the starting voltage of C-0.840 V to the fully transform voltage of C-2.500 V. This result highly supports our conclusion from operando XAS. The component at each discharged and charged voltages during ex situ XAS, operando XAS, and operando XRD are summarized in Table S2 (Supporting Information). The comparison indicates that operando study is important to understand the real-time discharge/charge process of BP in LIBs.
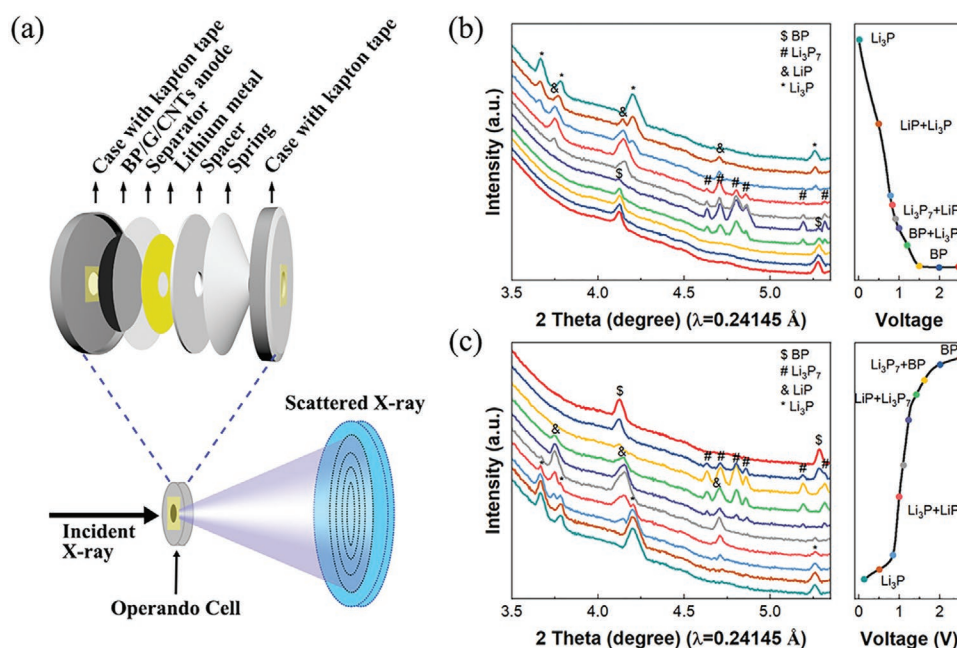

Figure 5. a) Schematic of the operando XRD measurement setup. Operando XRD spectra of BP/G/CNTs electrode during b) discharge (from bottom to top) and c) charge (from bottom to top).

3. Conclusion

We have developed a composite structure of nanosized BP, graphite, and carbon nanotubes by planetary ball-milling as an anode material for LIBs and understood the reaction mechanism of BP and Li$^+$ during cycling by ex situ and in situ synchrotron-based techniques. The introduction of graphite and CNTs can improve the electrical conductivity of the composite, offer pathways for Li$^+$ transport, and stabilize the structure of BP/G/CNTs during cycling. The nanosized BP together with graphite can accommodate the volume changing issue of BP during charge and discharge, avoiding pulverization of the material. The novel and unique BP/G/CNTs composite delivers an initial reversible capacity of 1375 mA h g^{-1} and still maintains 1031.7 mA h g^{-1} after 450 cycles, showing a remarkable capacity and stability. Moreover, the BP/G/CNTs anode shows excellent high current performance with capacities of 1009.4 mA h g^{-1} after 600 cycles at 0.5 A g^{-1}, 996 mA h g^{-1} after 1000 cycles at 1 A g^{-1}, 719 mA h g^{-1} after 1000 cycles at 2 A g^{-1}, and 508.1 mA h g^{-1} after 3000 cycles at 2 A g^{-1}. Moreover, by combining the results from ex situ XRD, ex situ XAS/XES, operando XRD, and operando XAS, we now have direct evidence to understand the reaction mechanism of BP-based anode materials for LIB systems. In general, BP reacts with Li$^+$ in three steps during discharge, forming Li$_3$P$_7$, LiP, and Li$_3$P at 1.119, 0.925, and 0.788 V, respectively. The reversible process can be observed during charge. The reverse conversions from Li$_3$P to LiP, subsequently to Li$_3$P$_7$, and finally to BP occurs at 1.028, 1.233, and 1.599 V during charge, respectively. In addition, by comparing the results between ex situ and operando XRD/XAS, we clearly reveal a small deviation in potentials for the occurrence of electrochemical intermediate species. Such offsite is likely due to the open-circuit relaxation effect of the ex situ electrode, indicating the importance and necessity of operando measurements in the studies of electrode materials in LIBs. In summary, the presented study not only demonstrates BP as a high-performance anode material in LIBs, but also illustrates the power of the operando synchrotron analyses in understanding the reaction mechanism of BP-based anode material with Li$^+$ during cycling, providing a feasible approach to study the electrochemical mechanism of other materials as well.

4. Experimental Section

Preparation of BP: 200 mg of red phosphorus (≥97%, trace metal basis, Sigma-Aldrich) was sealed in an evacuated quartz ampoule with 31.7 mg of Sn (99.995%, metal basis, Alfa Aesar) and 13.5 mg of I$_2$ (99.999%, metal basis, Alfa Aesar). The pressure of the ampoule was maintained below 10^{-3} mbar. The quartz ampoule was then placed in the middle of a tube furnace. After heating to 650 °C in 8 h, the temperature was maintained for 5 h and then slowly cooled down to 550 °C and kept at this temperature for another 6 h. Afterward, it was cooled down to 500 °C, maintaining at this temperature for 8 h. In the last step, the furnace was finally cooled in the ambient to room temperature in 30 h. The final product BP was obtained.

Preparation of BP/G/CNTs Composite: The BP/G/CNTs composite was synthesized through a ball-milling approach. The raw materials BP, graphite flakes, and single-walled CNTs (diameter: ≈2 nm) were mixed and sealed in a ZrO$_2$ jar in an Ar-filled glove box at the ratio of 5:4:1 with ZrO$_2$ balls (mass ratio of mixture and balls = 1:20). The mixture was then transferred to a planetary ball-milling machine (Retsch, PM 200)

and ball-milled for 120 h at the speed of 550 rpm. The composite, BP/G/CNTs, was then obtained.

Preparation of BP/G and BP/CNTs: The BP/G and BP/CNTs were prepared by the same ball-milling procedure as BP/G/CNTs but with the weight ratios of BP:graphite = 5:5 or BP:CNTs = 5:5.

Characterization: The morphology of BP/G/CNTs was investigated using a Hitachi S-4800 field-emission scanning electron microscope equipped with energy dispersive spectroscopy and TEM/HR-TEM. The structure of BP/G/CNTs before cycling was characterized by XRD at the Very Sensitive Elemental and Structural Probe Employing Radiation from a Synchrotron beamline of the Canadian Light Source (CLS) in Saskatoon, Saskatchewan, Canada using 11 keV X-rays (λ = 1.12276 Å). The structure of BP/G/CNTs after discharge and charge to different voltages were measured at Bruker AXS D8 Advance XRD with Cu Kα radiation (λ = 1.54178 Å). The operando XRD spectra during cycling were collected with the X-ray wavelength of 0.24145 Å at the beamline 17-BM of the Advanced Photon Source, Argonne National Laboratory. Raman spectra were measured with a HORIBA Scientific LabRAM HR Raman spectrometer operated with an incident laser beam at 532.03 nm. The ex situ and operando XAS and ex situ XES measurements were carried out at Soft X-ray Microcharacterization Beamline at CLS. The XES was a Rowland Circle design (easyXAFS) with the spectrometer housed inside a glove box, suitable for air sensitive materials and device.[38,39] It was specifically tuned to collect P and S K$_\alpha$ and K$_\beta$ emission with high efficiency and an energy resolution of <1 eV.

Electrochemical Characterization: The BP/G/CNTs (80 wt%) composite was mixed with acetylene black (10 wt%) and poly(vinylidene fluoride) binder (10 wt%) by *N*-methyl-2-pyrrolidone (NMP) to make a homogeneous slurry. The slurry was then coated onto a Cu foil with the thickness of 100 µm. The foil with the slurry was then heated under 60 °C for 7 h to remove NMP. The mass loading of the electrodes was 0.8–1.2 mg cm^{-1}.[2] The 2032 coin cell for electrochemical testing was assembled in an Ar-filled glove box with the BP-based anodes, Li metal reference electrode, and electrolyte (1 m LiPF$_6$ and 2% fluoroethylene carbonate (FEC) in a mixture of ethylene carbonate (EC) and diethyl carbonate (DEC), 1:1 in volume ratio). The separator was Celgard 2400 membrane. The galvanostatic charge–discharge tests for lithium-ion batteries conducted were between 0.001 and 2.5 V.

Supporting Information

Supporting Information is available from the Wiley Online Library or from the author.

Acknowledgements

Conflict of Interest

The authors declare no conflict of interest.

[1] W. Sun, X. Tang, Y. Wang, *Electrochem. Energy Rev.* **2020**, *3*, 127.

[2] F. Dou, L. Shi, G. Chen, D. Zhang, *Electrochem. Energy Rev.* **2019**, *2*, 149.

[3] Y. Kim, Y. Park, A. Choi, N. S. Choi, J. Kim, J. Lee, J. H. Ryu, S. M. Oh, K. T. Lee, *Adv. Mater.* **2013**, *25*, 3045.

[4] X. Han, M. Ouyang, L. Lu, J. Li, *J. Power Sources* **2014**, *268*, 658.

[5] M. Mayo, K. J. Griffith, C. J. Pickard, A. J. Morris, *Chem. Mater.* **2016**, *28*, 2011.

[6] W. Li, Z. Yang, M. Li, Y. Jiang, X. Wei, X. Zhong, L. Gu, Y. Yu, *Nano Lett.* **2016**, *16*, 1546.

[7] W. Li, Z. Yang, Y. Jiang, Z. Yu, L. Gu, Y. Yu, *Carbon* **2014**, *78*, 455.

[8] C. Marino, L. Boulet, P. Gaveau, B. Fraisse, L. Monconduit, *J. Mater. Chem.* **2012**, *22*, 22713.

[9] L. Wang, X. He, J. Li, W. Sun, J. Gao, J. Guo, C. Jiang, *Angew. Chem.* **2012**, *124*, 9168.

[10] C. Marino, A. Debenedetti, B. Fraisse, F. Favier, L. Monconduit, *Electrochem. Commun.* **2011**, *13*, 346.

[11] D. Yuan, J. Cheng, G. Qu, X. Li, W. Ni, B. Wang, H. Liu, *J. Power Sources* **2016**, *301*, 131.

[12] J. Qian, D. Qiao, X. Ai, Y. Cao, H. Yang, *Chem. Commun.* **2012**, *48*, 8931.

[13] Z. Yu, J. Song, M. L. Gordin, R. Yi, D. Tang, D. Wang, *Adv. Sci.* **2015**, *2*, 1400020.

[14] K. Hembram, H. Jung, B. C. Yeo, S. J. Pai, S. Kim, K.-R. Lee, S. S. Han, *J. Phys. Chem. C* **2015**, *119*, 15041.

[15] P. Yasaei, B. Kumar, T. Foroozan, C. Wang, M. Asadi, D. Tuschel, J. E. Indacochea, R. F. Klie, A. Salehi-Khojin, *Adv. Mater.* **2015**, *27*, 1887.

[16] G.-L. Xu, Z. Chen, G.-M. Zhong, Y. Liu, Y. Yang, T. Ma, Y. Ren, X. Zuo, X.-H. Wu, X. Zhang, *Nano Lett.* **2016**, *16*, 3955.

[17] J. Sun, G. Zheng, H.-W. Lee, N. Liu, H. Wang, H. Yao, W. Yang, Y. Cui, *Nano Lett.* **2014**, *14*, 4573.

[18] S. Haghighat-Shishavan, M. Nazarian-Samani, M. Nazarian-Samani, H.-K. Roh, K.-Y. Chung, B.-W. Cho, S. F. Kashani-Bozorg, K.-B. Kim, *J. Mater. Chem. A* **2018**, *6*, 10121.

[19] H. Jin, S. Xin, C. Chuang, W. Li, H. Wang, J. Zhu, H. Xie, T. Zhang, Y. Wan, Z. Qi, *Science* **2020**, *370*, 192.

[20] L.-Q. Sun, M.-J. Li, K. Sun, S.-H. Yu, R.-S. Wang, H.-M. Xie, *J. Phys. Chem. C* **2012**, *116*, 14772.

[21] C. M. Park, H. J. Sohn, *Adv. Mater.* **2007**, *19*, 2465.

[22] S. C. Jung, Y.-K. Han, *J. Phys. Chem. C* **2015**, *119*, 12130.

[23] W. Li, M. Li, Y. Hu, J. Lu, A. Lushington, R. Li, T. Wu, T. K. Sham, X. Sun, *Small Methods* **2018**, *2*, 1700341.

[24] F. Lin, Y. Liu, X. Yu, L. Cheng, A. Singer, O. G. Shpyrko, H. L. Xin, N. Tamura, C. Tian, T.-C. Weng, *Chem. Rev.* **2017**, *117*, 13123.

[25] W. Li, X. Sun, Y. Yu, *Small Methods* **2017**, *1*, 1600037.

[26] N. Liu, Z. Lu, J. Zhao, M. T. McDowell, H.-W. Lee, W. Zhao, Y. Cui, *Nat. Nanotechnol.* **2014**, *9*, 187.

[27] M. Köpf, N. Eckstein, D. Pfister, C. Grotz, I. Krüger, M. Greiwe, T. Hansen, H. Kohlmann, T. Nilges, *J. Cryst. Growth* **2014**, *405*, 6.

[28] K. Sa, P. C. Mahakul, B. Subramanyam, J. Raiguru, S. Das, I. Alam, P. Mahanandia, *IOP Conf. Ser.: Mater. Sci. Eng.* **2018**, *338*, 012055.

[29] B. Yang, B. Wan, Q. Zhou, Y. Wang, W. Hu, W. Lv, Q. Chen, Z. Zeng, F. Wen, J. Xiang, *Adv. Mater.* **2016**, *28*, 9408.

[30] A. Sayah, F. Habelhames, A. Bahloul, B. Nessark, Y. Bonnassieux, D. Tendelier, M. El Jouad, *J. Electroanal. Chem.* **2018**, *818*, 26.

[31] Z. Guo, H. Zhang, S. Lu, Z. Wang, S. Tang, J. Shao, Z. Sun, H. Xie, H. Wang, X. F. Yu, *Adv. Funct. Mater.* **2015**, *25*, 6996.

[32] S. Reich, C. Thomsen, *Philos. Trans. R. Soc. London, Ser. A* **2004**, *362*, 2271.

[33] J. Zhang, Z. Xie, W. Li, S. Dong, M. Qu, *Carbon* **2014**, *74*, 153.

[34] C. Peng, H. Chen, G. Zhong, W. Tang, Y. Xiang, X. Liu, J. Yang, C. Lu, Y. Yang, *Nano Energy* **2019**, *58*, 560.

[35] G. Nicotra, A. Politano, A. Mio, I. Deretzis, J. Hu, Z. Mao, J. Wei, A. La Magna, C. Spinella, *Phys. Status Solidi B* **2016**, *253*, 2509.

[36] J. Prietzel, J. Thieme, D. Paterson, *J. Plant Nutr. Soil Sci.* **2010**, *173*, 805.

[37] S.-M. Bak, Z. Shadike, R. Lin, X. Yu, X.-Q. Yang, *NPG Asia Mater.* **2018**, *10*, 563.

[38] M. Shakouri, W. M. Holden, Y. Hu, Q. Xiao, R. Igarashi, B. Schreiner, M. Bree, M. Li, W. Li, X. Sun, T.-K. Sham, *Electron. Struct.* **2020**, *2*, 047001.

[39] W. M. Holden, O. R. Hoidn, A. S. Ditter, G. T. Seidler, J. Kas, J. L. Stein, B. M. Cossairt, S. A. Kozimor, J. Guo, Y. Ye, M. A. Marcus, S. Fakra, *Rev. Sci. Instrum.* **2017**, *88*, 073904.